An adaptive isogeometric analysis meshfree collocation method for elasticity and frictional contact problems

Nguyen‐Thanh, Nhon; Li, Weidong; Huang, Jiazhao; Srikanth, Narasimalu; Zhou, Kun

2019

Nguyen-Thanh, N., Li, W., Huang, J., Srikanth, N., & Zhou, K. (2019). An adaptive isogeometric analysis meshfree collocation method for elasticity and frictional contact problems. International Journal for Numerical Methods in Engineering, 120(2), 209-230. doi;http://dx.doi.org/10.1002/nme.6132

https://hdl.handle.net/10356/103298

https://doi.org/10.1002/nme.6132

INTERNATIONAL JOURNAL FOR NUMERICAL METHODS IN ENGINEERING
Int. J. Numer. Meth. Engng 2019; **00**:1–25
Published online in Wiley Online Library (www.onlinelibrary.wiley.com). DOI: 10.1002/nme.6132

An adaptive isogeometric analysis meshfree collocation method for elasticity and frictional contact problems

Nhon Nguyen-Thanh[a]*, Weidong Li[b], Jiazhao Huang[b], Narasimalu Srikanth[c], Kun Zhou[b]*

[a] *School of Electrical and Electronic Engineering, Nanyang Technological University, 50 Nanyang Ave, Singapore*
[b] *School of Mechanical and Aerospace Engineering, Nanyang Technological University, 50 Nanyang Ave, Singapore*
[c] *Energy Research Institute, Nanyang Technological University, 50 Nanyang Ave, Singapore 639798, Singapore*

SUMMARY

A collocation method has been recently developed as a powerful alternative to Galerkin's method in the context of isogeometric analysis, characterized by significantly reduced computational cost, but still guaranteeing higher order convergence rates. In this work, we propose a novel adaptive isogeometric analysis meshfree collocation (IGAM-C) for the two-dimensional elasticity and frictional contact problems. The concept of the IGAM-C method is based upon the correspondence between the isogeometric collocation and reproducing kernel meshfree approach, which facilitates the robust mesh adaptivity in isogeometric collocation. The proposed method reconciles collocation at the Greville points via the discretization of the strong form of the equilibrium equations. The adaptive refinement in collocation is guided by the gradient-based error estimator. Moreover, the resolution of the nonlinear equations governing the contact problem is derived from a strong form to avoid the disadvantages of numerical integration. Numerical examples are presented to demonstrate the effectiveness, robustness and straightforward implementation of the present method for adaptive analysis.

Received . . .

KEY WORDS: Adaptive, Isogeometric Analysis, Meshfree Method, Collocation, Contact Mechanics

1. INTRODUCTION

Meshfree methods are viewed as next-generation computational techniques for problems involving large deformation, fracture and fragmentation and contact problems [1, 2, 3, 4, 5, 6]. Since the meshfree methods do not rely on a fixed topological connectivity between nodes, they are expected to be more adaptive and robust in resolving the problems where the classic grid-based methods are not suitable. Compared to the finite element method (FEM), meshfree methods are able to save computational time by avoiding re-meshing after each crack extension. Nevertheless, the meshfree method usually has less computational efficiency than the FEM, as higher computational cost is required for meshfree interpolation and numerical integration.

*Correspondence to: Email addresses: thanhnhon@ntu.edu.sg (N. Nguyen-Thanh), kzhou@ntu.edu.sg (K. Zhou)

The isogeometric analysis (IGA) was first proposed by Hughes *et al.* [7] as a powerful and reliable tool for computation and simulation of engineering problems. By adopting the non-uniform rational B-splines (NURBS) which are widely used in computer-aided designs as basis functions, IGA is not only applicable to engineering analyses but also capable of delivering accuracies superior to the standard FEM in many applications including contact mechanics. Recent attempts to solve contact problems within the IGA framework [8, 9, 10, 11, 12, 13] demonstrated significant advantages of IGA over conventional FEM, especially for the contact problems involving large deformations and large sliding. The exact geometry of contact surfaces can be smoothly represented by IGA to eliminate the geometry discontinuities caused by facet-based discretization. Besides, NURBS based IGA elements are less sensitive to the intense element distortions induced by the large deformation [14]. However, it is difficult to locally refine the NURBS patch due to its tensor product nature, which leads to an excessive overhead of control points with increasing refinement. With the goal of overcoming the limitations of NURBS for IGA, adaptive IGA has been studied with T-splines [15, 16], PHT-splines [17, 18, 19], hierarchical B-splines [20, 21], LR-splines [22] and hierarchical refinement [23, 24]. However, constraint equations are required in tandem with these methods, increasing the complexity and effort in their implementation.

Within the isogeometric collocation (IGA-C) context, several strategies have been studied to reduce the computational cost for Galerkin methods by using higher-order isogeometric basis functions [25, 26, 27, 28]. On one hand, exploiting the properties of the NURBS shape functions allows for integration rules with fewer integration points, e.g. 4 integration points instead of 9 for a two-dimensional (2D) element with a polynomial order of 3 [29]. A much higher increase in computational efficiency has been achieved through the collocation method. The strong form of the problem is enforced across a set of discrete collocation points that are equal to the number of control points. Although the number of computations per collocation point may be different from that per Gauss point, the collocation method saves a significant computational cost for higher-order shape functions [30]. Isogeometric collocation methods also eliminate the need for ad hoc hourglass stabilization techniques. Moreover, they show great promise for the development of accurate higher-order time integration schemes due to the convergence of high modes in the eigenspectrum. The discontinuous contact problem is generally very challenging for Galerkin methods [31, 32, 33, 34], whereas it can be effectively tackled by collocation methods. Recently, the enhanced collocation method proposed by Lorenzis *et al.* [35] which restores robustness and accuracy for general Neumann boundary conditions by emulating the integral Galerkin formulation on the domain boundaries. Kruse *et al.* [36] extended this work to large deformation frictional contact problems by using the two-half-pass formulation [37, 38] which seems to be the most natural algorithm in the collocation framework.

In this paper, a novel adaptive isogeometric analysis meshfree collocation method (IGAM-C) for 2D elasticity and frictional contact problems is investigated. The reproducing kernel meshfree is blended with isogeometric collocation, which provides the flexibility of meshfree adaptive refinement for isogeometric collocation. The formulation procedure is also simple and straight forward, as integration is not required in the formulation procedure. Moreover, the adaptivity scheme adopted in this work uses the gradient based error estimator which is robust and efficient. The purpose of this paper is two-fold. Firstly, the IGAM-C scheme for the numerical solution of linear steady state elasticity equations is developed with respect to their strong forms. The features of the IGAM-C method can facilitate an easier implementation of adaptive analysis. The computational efficiency of adaptive refinement and a high convergence rate can be achieved. Secondly, the present method is applied to 2D frictional contact problems with large deformation. The penalty method is regularized for the frictional contact constraints. The simulation results are in good agreement with the analytical solutions.

The paper is structured as follows. A brief introduction of meshfree and isogeometric approximants is given in Section 2. Section 3 presents the isogeometric and meshfree coupling approach within the framework of reproducing conditions. Section 4 elaborates the foundations of the linear elasticity collocation. Section 5 describes the formulation of the frictional contact

problem. Section 6 describes the gradient-based error estimation strategy. Section 7 explores various numerical examples. We finally close our paper with concluding remarks.

2. ISOGEOMETRIC ANALYSIS AND MESHFREE APPROXIMANTS

2.1. Isogeometric analysis

The B-spline basis functions $N_{i,p}(\xi)$ of order $q = 0$ (piece-wise constant) are defined recursively on the corresponding knot vector as follows:

$$N_{i,q}(\xi) = \begin{cases} 1 \text{ if } \xi_i \leq \xi \leq \xi_{i+1} \\ 0 \qquad \text{otherwise} \end{cases} , \tag{1}$$

$$N_{i,q}(\xi) = \frac{\xi - \xi_i}{\xi_{i+q} - \xi_i} N_{i,q-1}(\xi) + \frac{\xi_{i+q+1} - \xi}{\xi_{i+q+1} - \xi_{i+1}} N_{i+1,q-1}(\xi) \quad (\text{for q} \geq 1) \ . \tag{2}$$

The NURBS surface is given by

$$\mathbf{S}(\xi, \eta) = \sum_{i=1}^{n} R_i(\xi, \eta) \mathbf{P}_i \ ; \quad R_i = \frac{N_i(\xi, \eta) w_i}{\sum_{\bar{i}=1}^{n} N_{\bar{i}}(\xi, \eta) w_{\bar{i}}} \ , \tag{3}$$

where $\mathbf{P}_i$ are the control points in a bidirectional control net, $N_i(\xi, \eta)$ are the B-spline basis functions and w_i are the weights.

2.2. Moving least-squares interpolation

Based on the moving least-squares (MLS) based meshfree methods [39, 40], the unknown function u is approximated by

$$u^h(\xi) = \mathbf{p}^{\mathrm{T}}(\xi) \mathbf{a}(\xi) , \tag{4}$$

where $\mathbf{p^T}(\xi) = \{p_1(\xi), p_2(\xi), ..., p_m(\xi)\}$ is a complete monomial basis; m denotes the number of terms in the basis; ξ are the parametric coordinates, and $\mathbf{a}(\xi)$ is a vector of unknown coefficients. A complete polynomial basis of order *q* is defined as follows:

$$\mathbf{p^T}(\xi) = \left\{\mathbf{1}, \xi, \eta, \xi^{\mathbf{2}}, \xi\eta, \eta^{\mathbf{2}}\right\} \qquad \text{quadratic basis } m = 6 \ . \tag{5}$$

The unknown coefficients $\mathbf{a}(\xi)$ can be determined by minimizing the weighted L_2 norm with a weighted function as follows

$$J(\mathbf{a}) = \sum_{i=1}^{nm} \bar{w}(\xi - \xi_i) \left[\mathbf{p}^{\mathrm{T}}(\xi_i) \mathbf{a}(\xi) - u_i\right]^2, \tag{6}$$

where nm is the number of nodes within the domain of node ξ in which the weight function $\bar{w}(\xi - \xi_i)$ cannot equal to zero, and u_i denotes the nodal parameter of *u* at $\xi = \xi_i$.

The weight function $\bar{w}(\xi - \xi_i)$ in Eq. (6) influences the smoothness property of MLS shape functions. The quartic splines weight function is given as follows:

$$\bar{w}(\xi - \xi_i) = \begin{cases} 1 - 6r^2 + 8r^3 - 3r^4 & (r \leq 1) \\ 0 & (r > 1) \end{cases} , \quad r = \frac{|\xi - \xi_i|}{d^I_{max}}, \quad d^i_{\max} = \lambda d_c \ , \tag{7}$$

where d^i_{max} is the support radius of the node ξ_i, d_c denotes the average nodal spacing, and λ represents the dimensionless size of the support domain.

By setting the derivatives of J with respect to $\mathbf{a}(\xi)$ to be zero, it is solved as follows:

$$\mathbf{A}(\xi) \mathbf{a}(\xi) = \mathbf{B}(\xi) \mathbf{u} , \tag{8}$$

where matrices $\mathbf{A}(\xi)$ and $\mathbf{B}(\xi)$ are defined by

$$\mathbf{A}(\xi) = \sum_{i=1}^{nm} \bar{w}(\xi - \xi_i)\, \boldsymbol{p}(\xi_i)\, \boldsymbol{p}^{\mathrm{T}}(\xi_i) \quad \text{and} \tag{9}$$

$$\mathbf{B}(\xi) = \begin{bmatrix} \bar{w}(\xi - \xi_1)\, p(\xi_1) & \bar{w}(\xi - \xi_2)\, p(\xi_2) & \cdots & \bar{w}(\xi - \xi_{nm})\, p(\xi_{nm}) \end{bmatrix} . \tag{10}$$

By substituting $\mathbf{a}(\xi)$ into Eq. (4), the meshfree approximation of the displacement can be expressed as follows:

$$u^h(\xi) = \sum_{i=1}^{nm} \varphi_i(\xi)\, u_i(\xi) = \boldsymbol{\varphi}(\xi)\, \mathbf{u}, \tag{11}$$

where the shape function $\boldsymbol{\varphi_i}(\xi)$ is defined by

$$\boldsymbol{\varphi_i}(\xi) = \sum_{j=1}^{m} \mathrm{p}_j(\xi) \left(A^{-1}(\xi)\, B(\xi)\right)_{ji} = \mathbf{p}^{\mathrm{T}}(\xi) \left(\mathbf{A}^{-1}\mathbf{B}\right)_i . \tag{12}$$

For reproducing the polynomial of complete order, the consistency condition for the meshfree approximation is given as follows:

$$\sum_{i=1}^{nm} \boldsymbol{\varphi_i}(\xi)\, \mathbf{p}(\xi_i) = \mathbf{p}(\xi) . \tag{13}$$

3. REPRODUCING KERNEL MESHFREE FORMULATION OF ISOGEOMETRIC BASIS FUNCTIONS

3.1. Reproducing conditions for B-spline basis functions

The one-dimensional (1D) consistency condition for B-spline basis functions is defined as

$$\sum_{i=1}^{n} N_i^p(\xi)\, \mathbf{p}\left(\xi_i^{[\cdot]}\right) = \mathbf{p}(\xi) \ , \tag{14}$$

where $\mathbf{p}\left(\xi_i^{[\cdot]}\right) = \left\{1,\ \xi_i^{[1]},\ \left(\xi_i^{[2]}\right)^2,\ \cdots,\ \left(\xi_i^{[p]}\right)^p\right\}^{\mathrm{T}}$ is the 1D reproducing point vector and the reproducing points $\xi_i^{[l]}$ $(l = 1,\ 2,\ \cdots,\ p)$ are computed as

$$\xi_i^{[l]} = \sqrt[l]{\frac{S_p^l\left[G_{i+1}^{i+p}\right]}{C_p^l}}, \qquad C_p^l = \frac{p!}{l!\,(p-l)!} . \tag{15}$$

The 2D consistency condition is obtained as follows:

$$\sum_{I=1}^{nb} N_i^{pq}(\xi)\, \mathbf{p}\left(\xi_i^{[\cdot]}\right) = \mathbf{p}(\xi) \ , \tag{16}$$

where the reproducing point vector is expressed as

$$\mathbf{p}^{\mathrm{T}}\left(\xi_i^{[\cdot]}\right) = \left\{1, \xi_i^{[1]}, \eta_i^{[1]}, \left(\xi_i^{[2]}\right)^2, \xi_i^{[1]}\eta_i^{[1]}, \left(\eta_i^{[2]}\right)^2, \cdots, \left(\xi_i^{[p]}\right)^p, \cdots, \left(\eta_i^{[q]}\right)^q\right\} , \tag{17}$$

$$\xi_i^{[1]} = \frac{\xi_{i+1} + \xi_{i+2}}{2} \quad \text{, and} \quad \xi_i^{[2]} = \sqrt{\xi_{i+1}\xi_{i+2}} . \tag{18}$$

The reproducing kernel formulation is defined as

$$\phi_i(\xi) = \mathbf{p}^T\left(\xi_i^{[\cdot]}\right)\bar{\mathbf{C}}^{-1}(\xi)\,\mathbf{p}(\xi)\,\bar{w}\left(\xi-\xi_i^{[1]}\right), \tag{19}$$

where the moment matrix is calculated as

$$\bar{\mathbf{C}}(\xi) = \sum_{i=1}^{nm}\mathbf{p}\left(\xi_i^{[\cdot]}\right)\mathbf{p}^T\left(\xi_i^{[\cdot]}\right)\bar{w}\left(\xi-\xi_i^{[1]}\right)\ . \tag{20}$$

The linear reproducing points $\xi_i^{[1]}$ are treated as meshfree nodes. The B-spline basis functions can be represented by Eq. (19) when the support size equals $(p+1)/2$.

The IGAM-C basis functions can be obtained by considering weights w as follows:

$$\Phi_i(\xi) = \frac{\phi_i(\xi)\,w_i}{\sum_{j=1}^{n}\phi_j(\xi)\,w_j}\ . \tag{21}$$

The derivatives of the basis functions are shown in Appendix A.

3.2. Meshfree local refinement procedure

Consider knot vectors, $\Xi_1 = \{0,0,0,1,2,3,3,3\}$, is defined to obtain the initial meshfree nodes in directions ξ that is calculated as $\xi^{[1]} = \left\{0,\frac{1}{2},\frac{3}{2},\frac{5}{2},3\right\}$. The initial isogeometric basis function and the reproducing kernel meshfree basis functions are shown in Fig. 1. After the subdivision at $\xi=\frac{3}{2}$, the meshfree nodes of the new knot vectors $\Xi_1 = \left\{0,0,0,1,\frac{3}{2},2,3,3,3\right\}$ are calculated as $\xi^{[1]} = \left\{0,\frac{1}{2},\frac{5}{4},\frac{7}{4},\frac{5}{2},3\right\}$. Fig. 2a illustrates the basis functions after the first step of mesh refinement. It is found that two new meshfree nodes, $\left(\frac{5}{4},\frac{7}{4}\right)$, have replaced the original node $\left(\frac{3}{2}\right)$. Fig. 2b shows the second level of mesh refinement at $\xi = 7/4$. The meshfree nodes of the new knot vectors $\Xi_1 = \left\{0,0,0,1,\frac{3}{2},\frac{7}{4},2,3,3,3\right\}$ are calculated as $\xi^{[1]} = \left\{0,\frac{1}{2},\frac{5}{4},\frac{13}{8},\frac{15}{8},\frac{5}{2},3\right\}$. The 2D basis functions at the initial and second level mesh refinement are shown in Fig. 3 and Fig. 4, respectively.

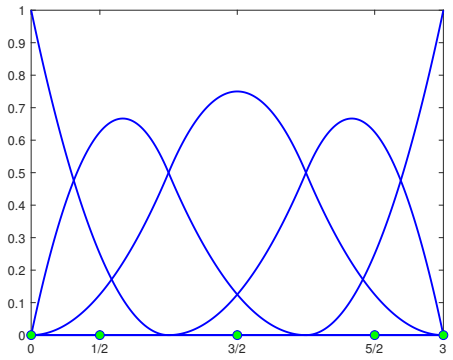

Figure 1. The initial basis functions in 1D with $\xi^{[1]} = \left\{0,\frac{1}{2},\frac{3}{2},\frac{5}{2},3\right\}$.

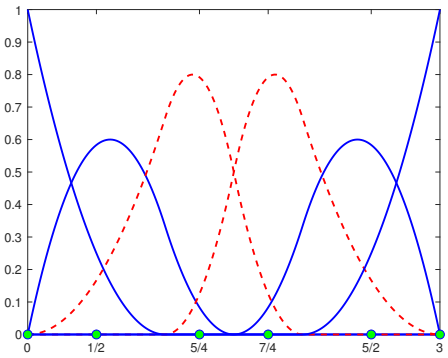

(a) $\xi^{[1]} = \{0, \frac{1}{2}, \frac{5}{4}, \frac{7}{4}, \frac{5}{2}, 3\}$

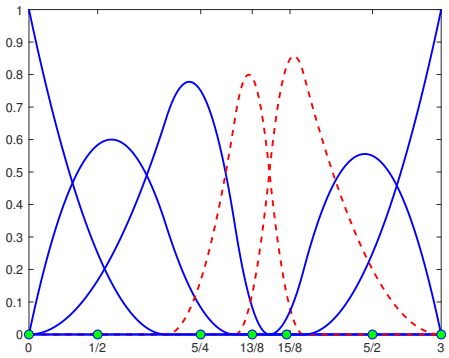

(b) $\xi^{[1]} = \{0, \frac{1}{2}, \frac{5}{4}, \frac{13}{8}, \frac{15}{8}, \frac{5}{2}, 3\}$

Figure 2. The basis functions in 1D: (a) first level refinement at $\xi = \frac{3}{2}$, and (b) second level refinement at $\xi = \frac{7}{4}$.

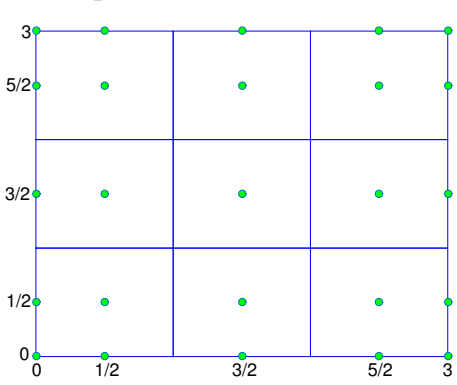

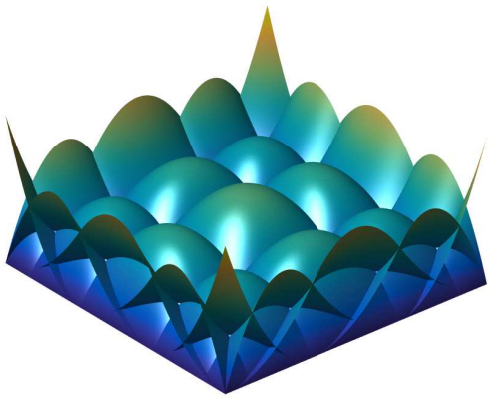

Figure 3. The basis functions at initial refinement mesh in 2D.

4. LINEAR ELASTOSTATICS

Let us assume a solid mechanics problem with linear elastic constitutive law and small displacements in the domain Ω bounded by Γ ($\Gamma = \Gamma^D \cup \Gamma^N$), as shown in Fig. 5. The equilibrium equation is given by

$$\nabla \cdot \boldsymbol{\sigma} + \mathbf{b} = 0 \qquad \text{in } \Omega\,, \tag{22}$$

where $\boldsymbol{\sigma}$ is the Cauchy stress tensor ($\boldsymbol{\sigma} = \sigma_{ij}\mathbf{e}_i \otimes \mathbf{e}_j$) and $\mathbf{b}$ a body force. The traction boundary condition is imposed as follows:

$$\boldsymbol{\sigma} \cdot \mathbf{n} = \bar{\mathbf{t}} \qquad \text{in } \Gamma^D\,, \tag{23}$$

where $\mathbf{n}$ is the outward unit normal to the boundary of the domain, and $\bar{\mathbf{t}}$ is the prescribed traction. The displacement boundary condition is given by

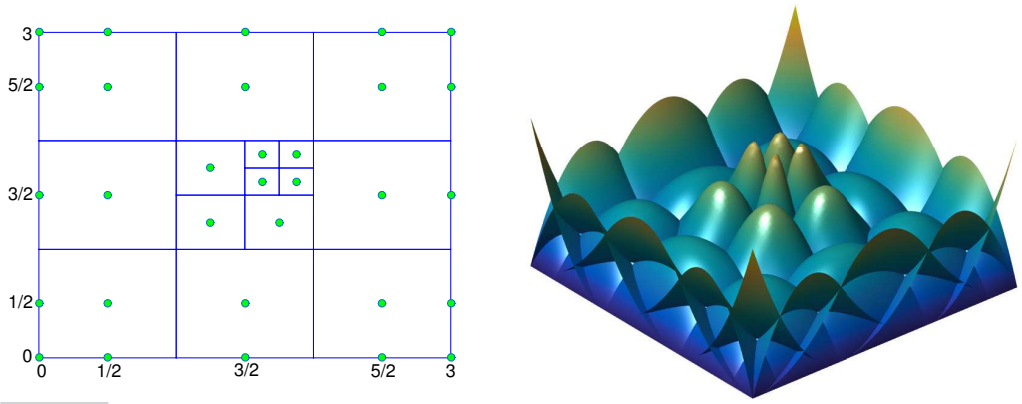

Figure 4. The basis functions at second level refinement ($\xi = \eta = 7/4$).

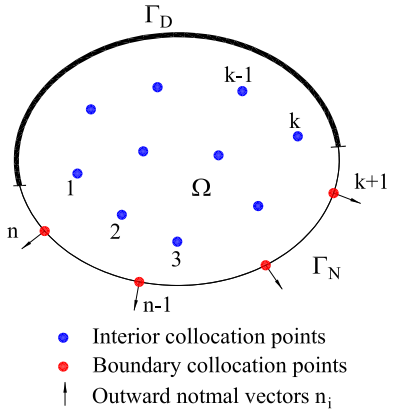

Figure 5. The collocation points in the reference configuration.

$$\mathbf{u} = \bar{\mathbf{u}} \qquad \text{in } \Gamma^N \ . \tag{24}$$

The constitutive law for a linear isotropic elastic material is given by

$$\boldsymbol{\sigma} = 2\mu\boldsymbol{\varepsilon} + \lambda \mathrm{tr}\left(\boldsymbol{\varepsilon}\right)\mathbf{1} \tag{25}$$

$$\boldsymbol{\varepsilon} = \frac{1}{2}\left(\nabla\mathbf{u} + \nabla\mathbf{u}^T\right) \ , \tag{26}$$

where $\boldsymbol{\varepsilon}$ is Cauchy's strain tensor, $\mathrm{tr}(\boldsymbol{\varepsilon})$ is the trace of the strain tensor and $\mathbf{1}$ is a second-order identity tensor ($\mathbf{1} = \delta_{ij}\mathbf{e}_i \otimes \mathbf{e}_j$). The Láme constants are

$$\lambda = \frac{\nu E}{1-\nu^2} \ , \quad \mu = G = \frac{E}{2\left(1+\nu\right)} \quad \text{(for plane stress)} \tag{27}$$

$$\lambda = \frac{\nu E}{\left(1+\nu\right)\left(1-2\nu\right)} \ , \quad \mu = G = \frac{E}{2\left(1+\nu\right)} \quad \text{(for plane strain)} \ , \tag{28}$$

where E is Young's modulus, G is the shear modulus, and μ is Poisson's ratio.

Within the isogeometric framework, we find an approximation $\mathbf{u}^h$ to the unknown exact solution field $\mathbf{u}$ of the elastostatic problem in the form

$$\mathbf{u}^h = \sum_{i=1}^{n} \Phi_i \mathbf{u}_i \tag{29}$$

where Φ_i are the IGAM-C basis functions, $\mathbf{u}_i$ are the unknown displacement control variables. The stiffness matrix, displacement and force vectors are given by

$$\begin{bmatrix} \mathbf{K}^i \\ \mathbf{K}^D \\ \mathbf{K}^N \end{bmatrix} \begin{pmatrix} \mathbf{u}^i \\ \mathbf{u}^D \\ \mathbf{u}^N \end{pmatrix} = \begin{pmatrix} \mathbf{f}^i \\ \mathbf{f}^D \\ \mathbf{f}^N \end{pmatrix} , \tag{30}$$

where

$$\begin{aligned} \mathbf{K}^i &= \mathcal{L}\left(\Phi_j\left(\xi_i\right)\right)\mathbf{u} \;;\quad \mathbf{f}^i = -\mathbf{b}\left(\xi_i\right) \quad \forall\left(\xi_i\right) \in \Omega \\ \mathbf{K}^D &= \mathbf{B}^D\left(\Phi_j\left(\xi_i\right)\right)\mathbf{u} \;;\quad \mathbf{f}^D = \bar{\mathbf{t}}\left(\xi_i\right) \quad \forall\left(\xi_i\right) \in \Gamma^D \\ \mathbf{K}^N &= \mathbf{B}^N\left(\Phi_j\left(\xi_i\right)\right)\mathbf{u} \;;\quad \mathbf{f}^N = \bar{\mathbf{u}}\left(\xi_i\right) \quad \forall\left(\xi_i\right) \in \Gamma^N \end{aligned} . \tag{31}$$

The operator matrices in the two-dimensional elasticity can be written as

$$\mathcal{L} = \begin{bmatrix} (\lambda+2\mu)\frac{\partial^2}{\partial x^2} + \mu\frac{\partial^2}{\partial y^2} & (\lambda+\mu)\frac{\partial^2}{\partial x \partial y} \\ (\lambda+\mu)\frac{\partial^2}{\partial x \partial y} & (\lambda+2\mu)\frac{\partial^2}{\partial y^2} + \mu\frac{\partial^2}{\partial x^2} \end{bmatrix} \tag{32}$$

$$\mathbf{B}^N = \begin{bmatrix} (\lambda+2\mu)\, n_x\frac{\partial}{\partial x} + \mu n_y\frac{\partial}{\partial y} & \lambda n_x\frac{\partial}{\partial y} + \mu n_y\frac{\partial}{\partial x} \\ \lambda n_y\frac{\partial}{\partial x} + \mu n_x\frac{\partial}{\partial y} & (\lambda+2\mu)\, n_y\frac{\partial}{\partial y} + \mu n_x\frac{\partial}{\partial x} \end{bmatrix} \tag{33}$$

$$\mathbf{B}^D = \begin{bmatrix} 1 & 0 \\ 0 & 1 \end{bmatrix} . \tag{34}$$

5. LARGE DEFORMATION CONTACT PROBLEM

In this section, the basics of frictional contact between two deformable bodies in a geometrically non-linear framework are presented. This includes normal and tangential contact traction, the differentiation between sticking and sliding, and the linearization of the contact traction.

5.1. Statement of the contact algorithms

Consider two elastic bodies that come into contact at some points of time during their deformation (see in Fig. 6). The two bodies will be distinguished in the sense that one surface will be denoted as the mortar surface (master) $\mathcal{B}^m$ and the other as the non-mortar surface (slave) $\mathcal{B}^s$. The relation between the initial configuration $\mathbf{X}^\alpha$, the displacements $\mathbf{u}^\alpha$ and the current configuration $\mathbf{x}^i$ is given by

$$\mathbf{x}^\alpha = \mathbf{u}^\alpha + \mathbf{X}^\alpha , \tag{35}$$

where α denotes the slave and master bodies, respectively.

In order to take interactions between the master body $\varphi\left(\mathcal{B}^m\right)$ and the slave body $\varphi\left(\mathcal{B}^s\right)$ into account, the location and the size of the contact boundary have to be known. The distance between a fixed point $\mathbf{x}^s$ on the contact boundary Γ_s of the slave surface and an arbitrary point $\mathbf{x}^m = \mathbf{x}^m\left(\xi\right)$ on the contact boundary of the master surface Γ^m is introduced by the function

$$d = \min_{\mathbf{x}^m \subseteq \Gamma^m} \left\|\mathbf{x}^s - \mathbf{x}^m\left(\xi\right)\right\| \tag{36}$$

On the master surface, the convective coordinates ξ^m are mapped onto the parametric coordinates of the surface and define the covariant vectors $\boldsymbol{\tau}_1 = \mathbf{x}^m_{,\xi}$. Using the metric $m_{11} := \boldsymbol{\tau}_1 \cdot \boldsymbol{\tau}_1$ with

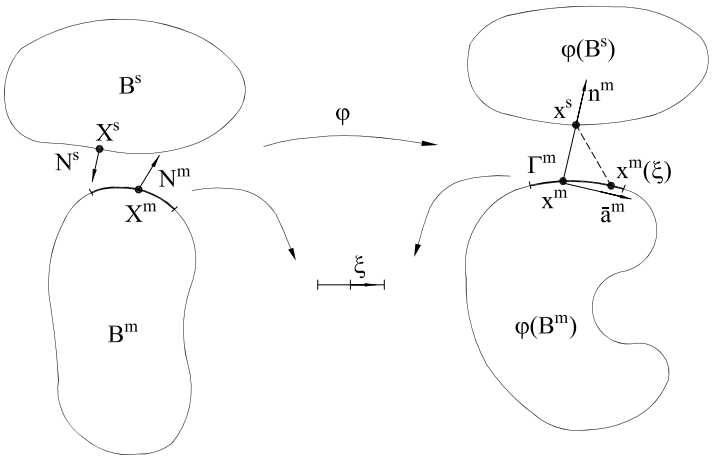

Figure 6. Geometrical magnitudes for the contact formulation.

inverse component m^{11}, the contravariant vector $\boldsymbol{\tau}^1 := m^{11}\boldsymbol{\tau}^1$ is induced. The curvature follows $k_{11} = \mathbf{x}^m_{,\xi\xi} \cdot \mathbf{n}$, where $\mathbf{n} = \mathbf{n}^m$ is the normal unit vector.
The residual of the closest point projection is given by

$$f(\xi) = \boldsymbol{\tau}_1(\xi) \cdot [\mathbf{x}^s - \mathbf{x}^m(\xi)] \ , \tag{37}$$

and this closest point vanishes at the projection point $\bar{\xi}$, i.e., $f\left(\bar{\xi}\right) = 0$.
The iterative process starting from a guess $\hat{\xi}$ requires the tangent

$$K_{11} = f_{,\xi} = \mathbf{x}^m_{,\xi\xi}(\xi) \cdot [\mathbf{x}^s - \mathbf{x}^m(\xi)] - m_{11}(\xi) \ . \tag{38}$$

The closest projection point and the related variables are usually defined in the literature with the notation $(\bar{\bullet})$, such as $\bar{\mathbf{x}}^m = \mathbf{x}^m\left(\bar{\xi}\right)$. In the following, we will denote a quantity's evaluation at the minimum distance point by a bar over its notation.
The outward unit normal on the master surface at the master point is given by

$$\bar{\mathbf{n}}^m = \frac{\mathbf{x}^s - \bar{\mathbf{x}}^m}{\|\mathbf{x}^s - \bar{\mathbf{x}}^m\|} = -\frac{\bar{\mathbf{a}}^m \times \bar{\mathbf{e}}_3}{\|\bar{\mathbf{a}}^m \times \bar{\mathbf{e}}_3\|} \ , \tag{39}$$

where $\bar{\mathbf{e}}_3$ is the unit vector orthogonal to the plane, and the tangent vector $\bar{\mathbf{a}}^m = \bar{\mathbf{x}}^m_{,1}$.

5.2. Contact variables and constraints

In this formulation a penalty function is introduced to enforce the contact constraints

$$p_n = \begin{cases} -\varepsilon_n g_n n^m & \text{for} \quad g_n < 0 \\ 0 & \text{for} \quad g_n \geq 0 \end{cases} \tag{40}$$

where ε_n is the penalty parameter and the normal gap between the two bodies is defined as

$$g_n = (\mathbf{x}^s - \mathbf{x}^m) \cdot \mathbf{n}^m \tag{41}$$

where $\mathbf{x}^s, \mathbf{x}^m$ are the coordinates of the collocation points in contact and the corresponding projection points on the other surface respectively; $\mathbf{n}^m$ is the surface normal at the contact collocation point.

The contact traction is composed of normal and tangential components

$$\mathbf{p} = -p_n \mathbf{n}^m + p_t^1 \boldsymbol{\tau}_1^m \tag{42}$$

where $\boldsymbol{\tau}_1^m$ are the covariant tangential vectors ($\boldsymbol{\tau}_1^m = \mathbf{x}^m_{,\xi}$).

For frictional contact, the tangential component is dependent on whether sticking or sliding occurs. The status of the contact, stick or slip, is determined by a trial function given by

$$\Phi^{\text{trial}} = \left\|\mathbf{p}_t^{\text{trial}}\right\| + \mu p_n \tag{43}$$

with

$$\mathbf{p}_t^{\text{trial}} = p_t^{1\text{trial}} \boldsymbol{\tau}_1^m \, . \tag{44}$$

The sticking constraint can be regularized by a penalty approach as follows:

$$p_t^1 = p_t^{1\text{trial}} = p_t^{1\text{old}} + \varepsilon_t \left(\bar{\xi}^m - \xi^{\text{old}}\right) \, . \tag{45}$$

Consequently, the tangential components in sticking or sliding are

$$p_t^1 = \begin{cases} p_t^{1\text{trial}} & \text{if } \Phi^{\text{trial}} \leq 0 \\ -\mu p_n \frac{p_t^{1\text{trial}}}{\left\|\mathbf{p}_t^{\text{trial}}\right\|} & \text{otherwise} \end{cases} \tag{46}$$

where for the sliding condition validity of the Coulomb's law has been assumed.

$$p_t^1 = -\mu p_n \frac{p_t^{1\text{trial}}}{\left\|\mathbf{p}_t^{\text{trial}}\right\|} \, , \tag{47}$$

where μ is the coefficient of friction. More details about the linearization and the consequent expression of the consistent tangent stiffness matrix are deferred to the Appendix B.

6. ADAPTIVE SCHEME

The IGAM-C possesses attractive features to facilitate an easier implementation for an adaptive scheme. Without the constraint of the nodal connectivity, additional nodes can be easily inserted into the meshes for local refinement, and the cumbersome remeshing process is also avoided.

6.1. Error estimator

In order to determine and refine the elements associated with large errors, the gradient-based error estimation strategy [41] is applied. To calculate the gradient of strain energy density, the following steps are implemented.

The strain energy density of an element e is calculated as

$$D_e^{SE} = \frac{1}{2}\sigma^T \varepsilon = \frac{1}{2}\mathbf{u}^T \mathbf{B}^T \mathbf{C}\mathbf{B}\mathbf{u} \, , \tag{48}$$

where σ and ϵ are the stress and strain vectors respectively. The averaged gradient of strain energy density for an element e is calculated as

$$G_e^{SED} = \frac{\sum_{i=1}^{N_e-1} \sum_{j=i+1}^{N_e} \frac{\left|D_i^{SE} - D_j^{SE}\right|}{l_{ij}}}{N_e!} \, . \tag{49}$$

where N_e is the number of nodes within an element k and l_{ij} is the distance between nodes i and j. The strain energy densities at nodes i and j are denoted by D_i^{SE} and D_j^{SE}, respectively.

The averaged mesh intensity of an element e is obtained by

$$r_e^{MI} = \frac{G_e^{SED}}{D_e^M} \tag{50}$$

A mesh density D_e^M that represents the number of nodes within a unit area is calculated as

$$D_e^M = \frac{N_e}{A_e} , \tag{51}$$

where A_e is the area of an element e.

6.2. *Refinement and stopping criteria*

To mark elements that need to be refined, the threshold R_{thre} is used. For elements with a higher averaged mesh intensity than the threshold, mesh refinement should be implemented within this element. Otherwise, the element remains constant. The refinement criteria can be expressed as

$$\text{if} \quad r_e^{MI} > R_{thre} \qquad \text{refine} \qquad (R_{\min} \leq R_{thre} \leq R_{\max}) \ .$$

Here, different thresholds R_{thre} may be chosen in different problems for obtaining both accurate and efficient solutions. The flow chart of the adaptive analysis is summarized in Fig. 7

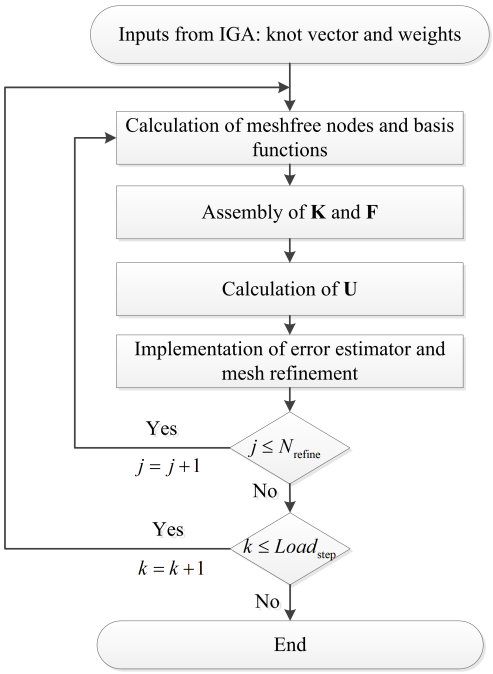

Figure 7. The flow chart for isogeomtric meshfree collocation with adaptive refinement.

7. NUMERICAL EXAMPLES

In this section, we present the performance of the proposed method through benchmark examples, considering both elasticity and large deformation contact problems. An intensive numerical study is carried out to verify the proposed method. The IGAM-C and IGA-C discretizations with the same global number of degree of freedom (DOF) and a quadratic polynomial $(p = 2)$ are employed for comparison purposes. The numerical effectiveness of the present method heavily relies on the robust computation of the strain energy in terms of the accuracy and computational cost.

7.1. Convergence studies

In the convergence studies, the error is studied as a function of the number of collocation points. The error in the displacement is calculated by

$$\|\text{err}\|_{L_2} = \frac{\|\mathbf{u} - \mathbf{u}_{\text{exact}}\|_{L_2}}{\|\mathbf{u}_{\text{exact}}\|_{L_2}} , \tag{52}$$

with

$$\|\mathbf{u}\|_{L_2} = \left(\int_\Omega \mathbf{u}^T \mathbf{u} d\Omega \right)^{1/2} . \tag{53}$$

The error in the strain energy is computed by

$$\|\text{err}\|_{E} = \frac{\|\mathbf{u} - \mathbf{u}_{\text{exact}}\|_{E}}{\|\mathbf{u}_{\text{exact}}\|_{E}} , \tag{54}$$

with

$$\|\mathbf{u}\|_{E} = \left(\int_\Omega (\boldsymbol{\varepsilon} - \boldsymbol{\varepsilon}_{\text{exact}})^T \mathbf{C} (\boldsymbol{\varepsilon} - \boldsymbol{\varepsilon}_{\text{exact}}) \, d\Omega \right)^{1/2} . \tag{55}$$

7.2. Linear elastostatics problems

7.2.1. A hollow cylinder As shown in Fig. 8a, we consider a hollow cylinder with an internal radius a of $1m$ and an external radius b of $4m$ being subjected to an internal pressure $p = 3 \times 10^4 kN/m^2$. Plane stress conditions are assumed with Young's modulus $E = 3 \times 10^7 kN/m^2$ and Poisson ratio $\nu = 0.25$. Symmetry conditions are imposed on the left and bottom edges while the outer boundary is traction free. The exact solution for the stress components [42] is given by

$$\sigma_r(r) = \frac{a^2 p}{b^2 - a^2} \left(1 - \frac{b^2}{r^2} \right) \; ; \; \sigma_\theta(r) = \frac{a^2 p}{b^2 - a^2} \left(1 + \frac{b^2}{r^2} \right) \; ; \; \sigma_{r\theta} = 0 , \tag{56}$$

whereas the radial and the tangential exact displacements are given by

$$u_r(r) = \frac{a^2 p r}{E(b^2 - a^2)} \left\{ 1 - \upsilon + \frac{b^2}{r^2}(1 + \upsilon) \right\} \; ; \quad u_\theta = 0 . \tag{57}$$

Starting from an initial parametrization of degree 2 with 72 DOFs (Fig. 8b), we obtained an adaptive mesh after 5 refinement steps as shown in Fig. 8c. Beside that, the uniform mesh of the IGA-C method is shown in Fig. 8d. The error in strain energy error norms is shown in Fig. 9. It is evident that the present method with uniform mesh achieves the same convergence rate as that obtained by the IGA-C method. Moreover, the present method with adaptive refinement achieves more accurate and efficient solutions than the IGA-C method. The number of DOFs required in the present method with the adaptivity is 4588, which is less than the 8712 required in the basic IGA-C method. The contour plot of displacement is also shown in Fig. 10.

7.2.2. Elastic plate with circular hole Consider the problem of an infinite plate with a circular hole of radius R loaded at infinity by a traction T_x in the x direction, as shown in Fig. 11a. The analytical solution of this problem is given by

$$\begin{aligned}
\sigma_{rr}(r,\theta) &= \frac{T_x}{2} \left(1 - \frac{R^2}{r^2} \right) + \frac{T_x}{2} \left(1 - 4\frac{R^2}{r^2} + 3\frac{R^4}{r^4} \right) \cos 2\theta \\
\sigma_{\theta\theta}(r,\theta) &= \frac{T_x}{2} \left(1 + \frac{R^2}{r^2} \right) - \frac{T_x}{2} \left(1 + 3\frac{R^4}{r^4} \right) \cos 2\theta \\
\sigma_{r\theta}(r,\theta) &= -\frac{T_x}{2} \left(1 + 2\frac{R^2}{r^2} - 3\frac{R^4}{r^4} \right) \sin 2\theta
\end{aligned} \tag{58}$$

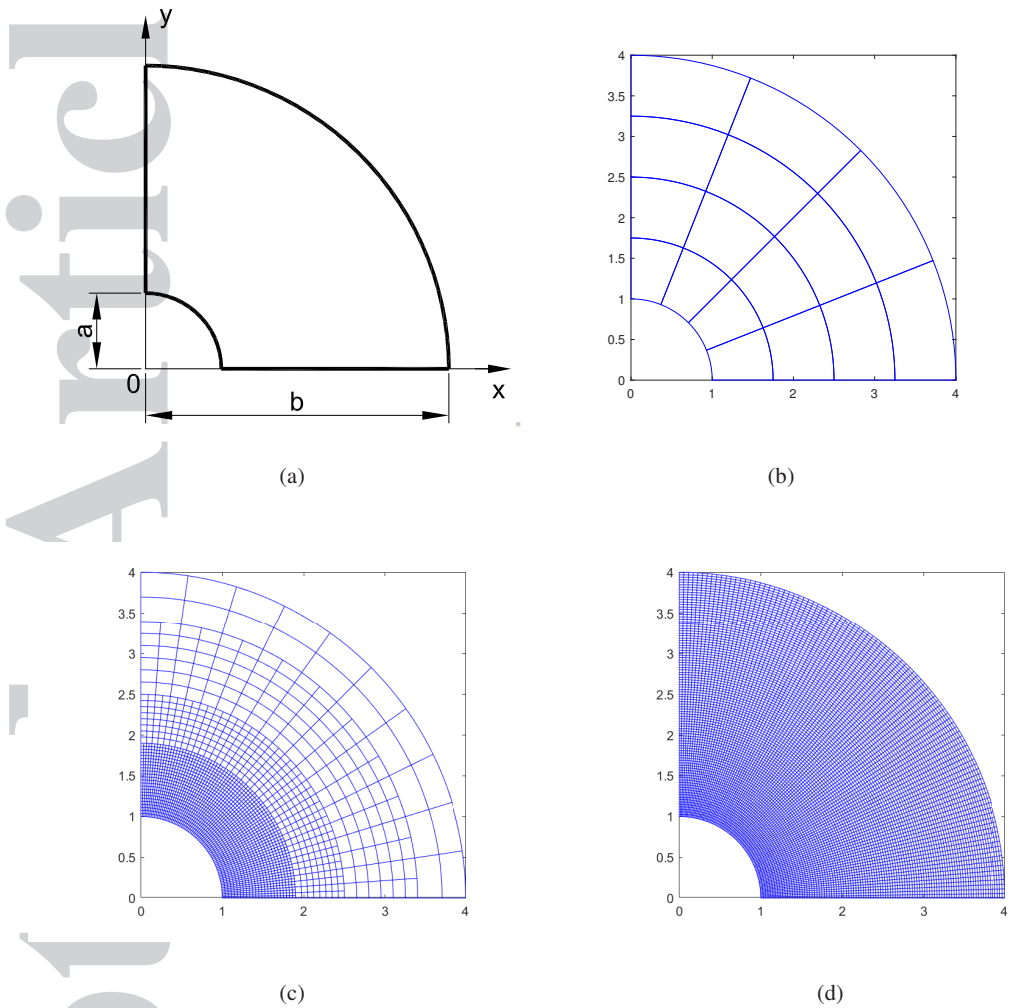

Figure 8. A hollow cylinder subjected to inner pressure and domain discretization: (a) geometrical modeling, (b) initial mesh, (c) adaptive mesh after 5 refinement steps, and (d) uniform mesh.

and (r, θ) is a polar co-ordinate system with the origin at the center of the hole.

Due to symmetry, only the upper right quadrant of the plate is modelled. A plane stress state is assumed with dimensionless elastic modulus $E = 1 \times 10^5$ and Poisson's ratio $\nu = 0.3$, T_x is assumed to be 1. Symmetry conditions are imposed on the right and bottom edges, while the inner boundary at $R = 1$ is traction free.

Fig. 11b,c,d show an initial mesh (with DOFs being 120), adaptive mesh refinement and uniform mesh respectively. The contour plot of stress components are shown in Fig. 12. Fig. 13 illustrates the convergence rate in terms of the error in energy norm. It is obvious that the present method offers the same convergence rate as that obtained by the basic isogeometric collocation in terms of uniform mesh. With respect to the DOFs used to achieve a certain accuracy, the present method is, as expected, superior to adaptive refinement with fewer DOFs. The number of DOFs needed by the present method with the adaptivity is 4432, which is less than the 17160 needed by the IGA-C method. Fig. 14 shows the efficiency of computation in terms of the error estimator versus computational cost. It can be seen that the present method is the most efficient while the isogeometric collocation is the least.

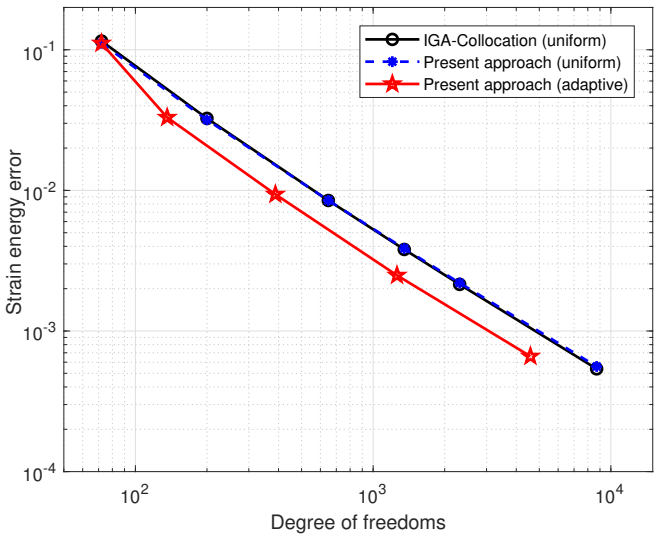

Figure 9. Convergence plot in the energy norm.

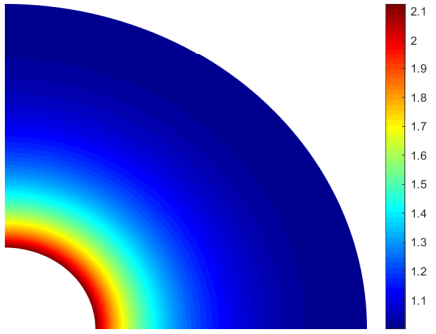

Figure 10. Contour plot in the displacement.

7.2.3. Hertzian contact The Hertz's problems are a typical benchmark in linear elasticity contact mechanics. In this work, we consider the problem of the contact of an infinite cylinder of radius $R = 1$ with a rigid plane (see Fig. 15a). The material of the cylinder is linear elastic with Young's modulus $E = 1.33$ and Poisson's ratio $\nu = 0.333$. The penalty parameters are $\epsilon_n = 10^4$, $\epsilon_t = 10^3$ and the coefficient of friction is $\mu = 0.3$. The cylinder is loaded by a vertical force $\bar{p} = 0.005$ applied as a uniformly distributed load on the upper surface. The analytical solution for this problem can be found in [43, 44].

As can be seen from Fig. 15b,c,d which show the uniform mesh, non-uniform mesh and adaptive mesh refinement respectively. Fig. 16 shows the contour plot of the stress σ_{yy}. Fig. 17 shows a comparison of the normal and tangential components of the contact traction, both normalized with respect to the normal contact traction at the midpoint of the contact area. It can be seen that, the contact traction predicted by the proposed contact formulation in isogeometric collocation agrees well with that given by the analytical solution. As shown in Fig. 18, the present method achieves a higher convergence rate than the IGA-C method with both uniform and non-uniform meshes. Moreover, the number of DOFs required in the present method is 5384, which is less than the 12000 and 38720 required in the IGA-C method with uniform and non-uniform meshes, respectively.

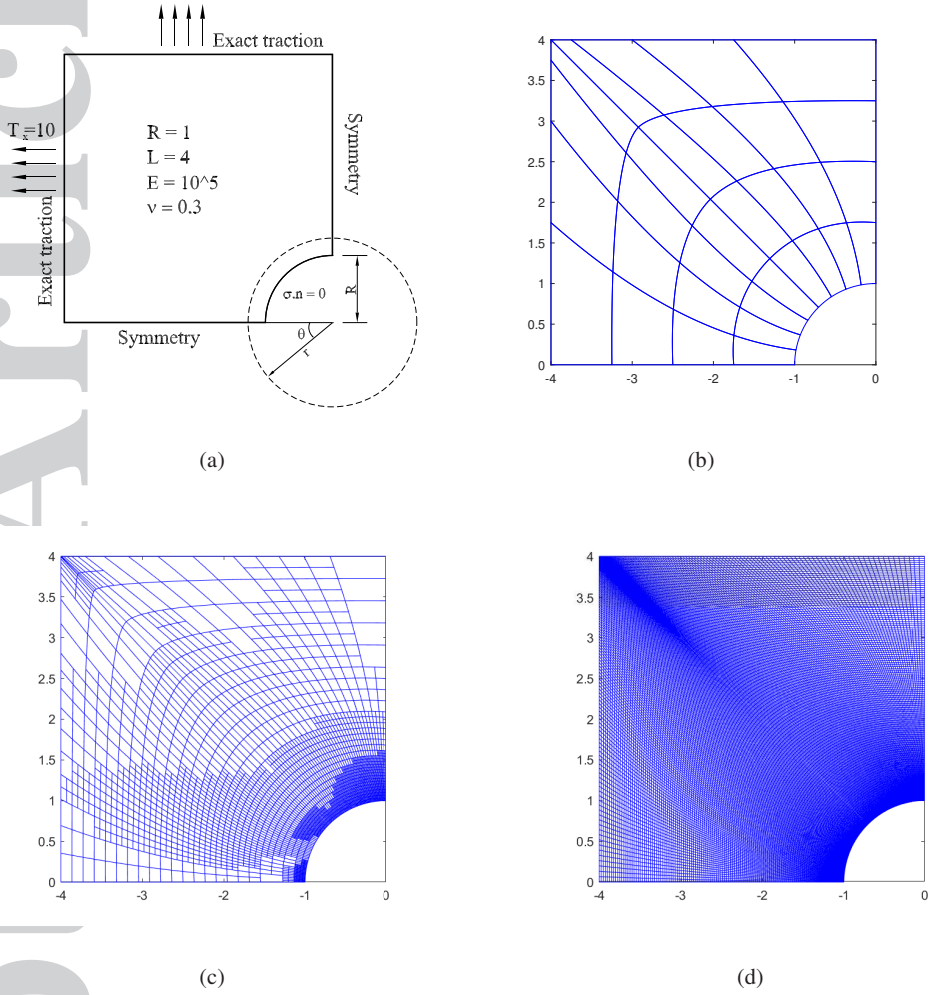

Figure 11. The elastic plate with a circular hole: (a) geometrical modeling, (b) initial mesh, (c) adaptive mesh after 5 refinement steps, and (d) uniform mesh.

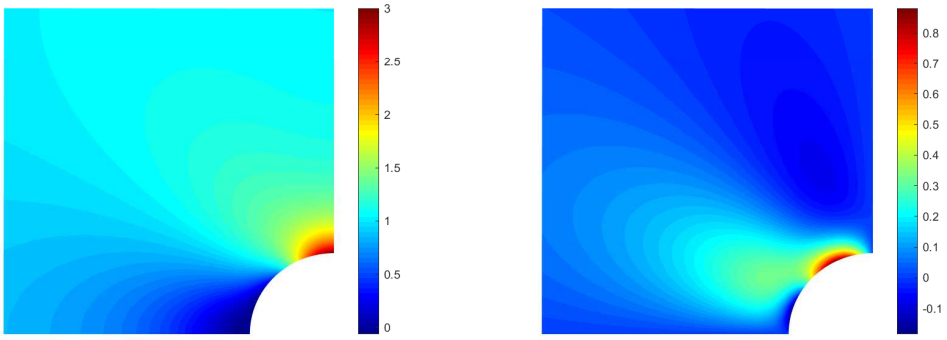

Figure 12. Stress field contour plots for σ_{xx} and σ_{xy}, respectively.

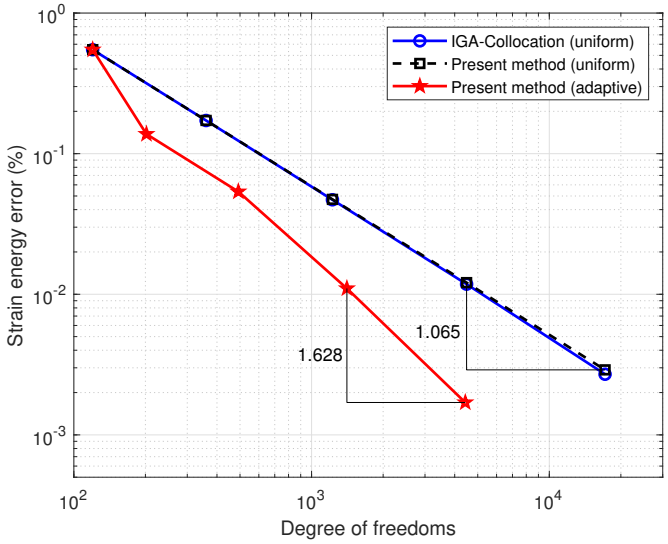

Figure 13. Convergence plot for the plate with circular hole.

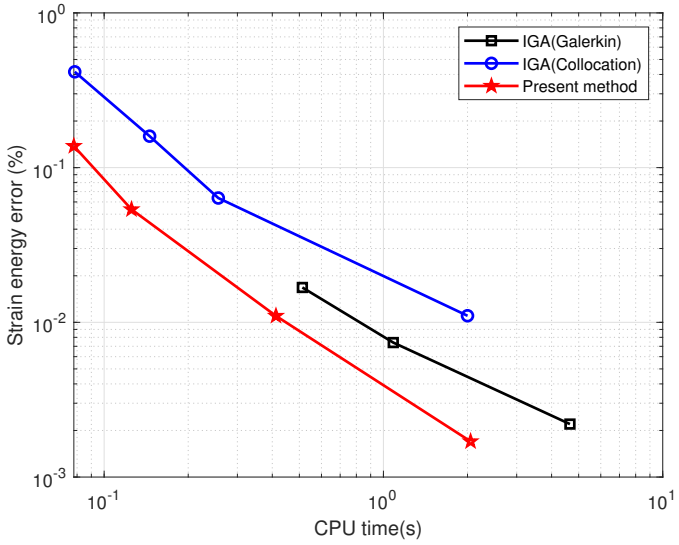

Figure 14. The comparison of the computational efficiency between IGAM-C and IGA-C.

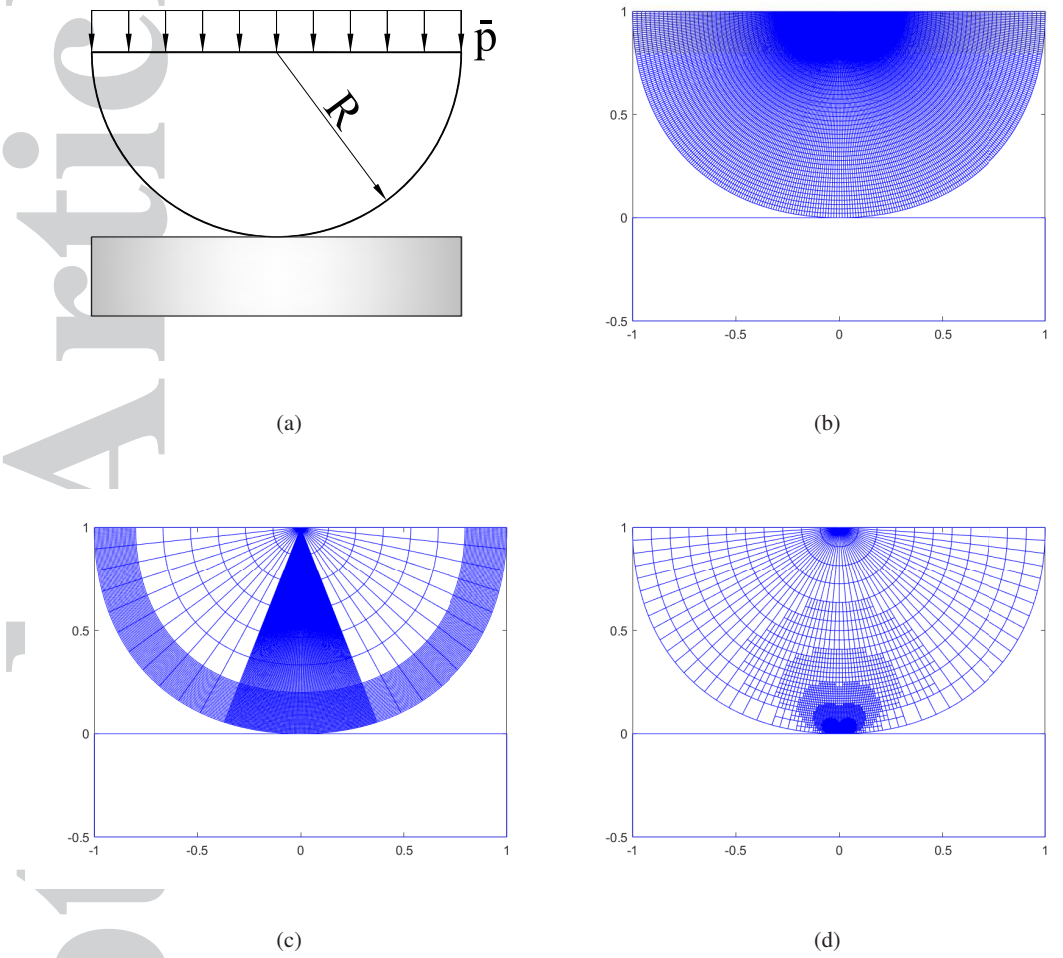

Figure 15. Hertzian contact problem: (a) geometrical configuration, (b) uniform mesh, (c) non-uniform mesh, and (d) adaptive mesh after 5 refinement steps.

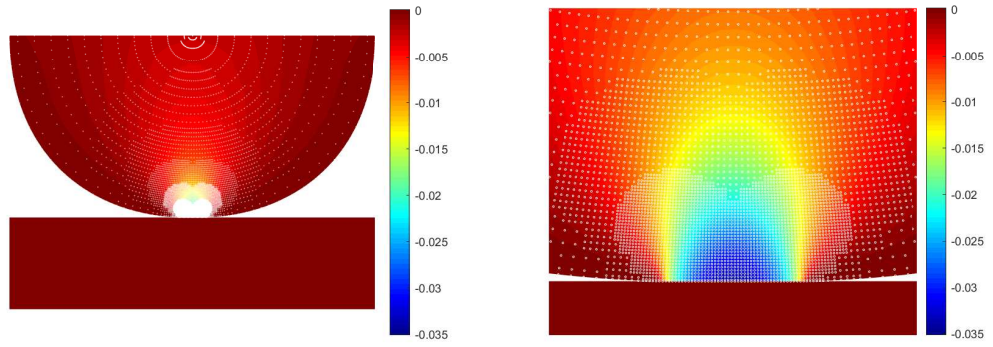

Figure 16. Distribution of the stress σ_{yy}, and close-up of the contact region.

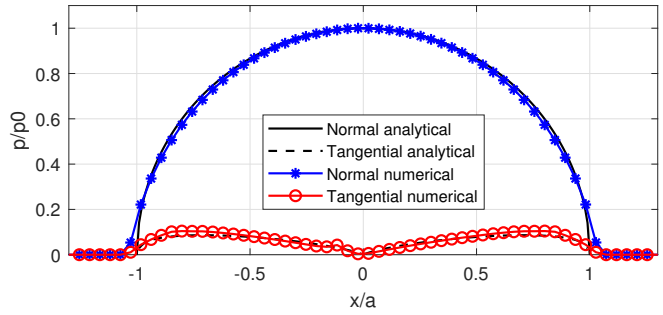

Figure 17. Analytical and numerical contact pressure (normal and tangential components).

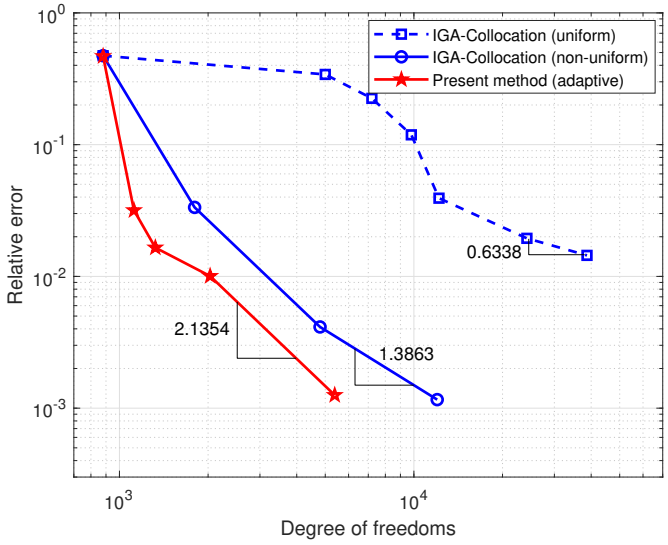

Figure 18. Convergence plot for the Hertz's problem.

7.3. *Hertz contact problem with friction between deformable bodies*

The schematic of this problem is shown in Fig. 19, where the values of the geometrical variables are $R = 1, b = 0.5, h = 0.3$. The materials of both bodies are linearly elastic with Young's modulus $E = 1$ and Poisson's ratio $\nu = 0.3$. The penalty parameters are $\varepsilon_N = 10^3$ and $\varepsilon_T = 10^2$, and the coefficient of friction is $\mu = 0.2$. The model is loaded with a vertical downward displacement $\hat{v} = 0.002$ and a horizontal displacement $\hat{u} = 0.00075$. The analytical solution for infinitesimal deformations can be found in [44].

Fig. 20 shows the final distribution of the stress σ_{yy}, whereas Fig. 21 compares numerical and analytical results in terms of normalized components of the contact traction versus normalized coordinates along the contact area. Once again excellent agreement is obtained.

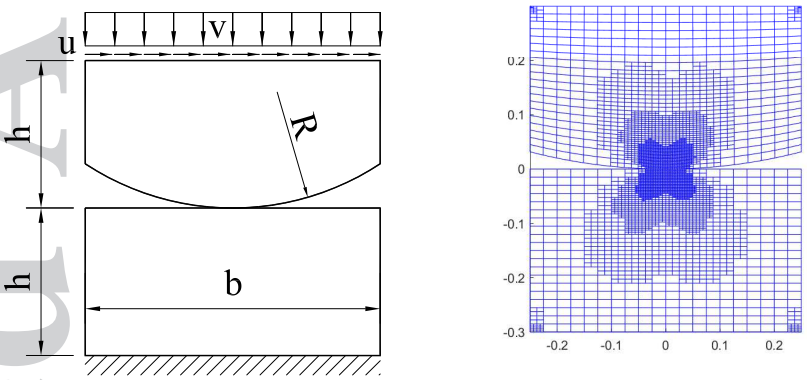

(a) (b)

Figure 19. (a) Schematic of the cylinder on plane Hertzian contact problem, and (b) adaptive mesh after 3 refinement steps.

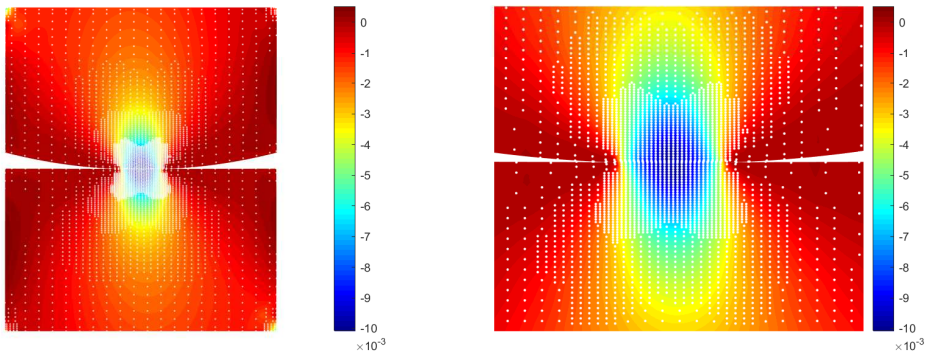

Figure 20. Contour plot of σ_{yy}, and close-up of the contact region.

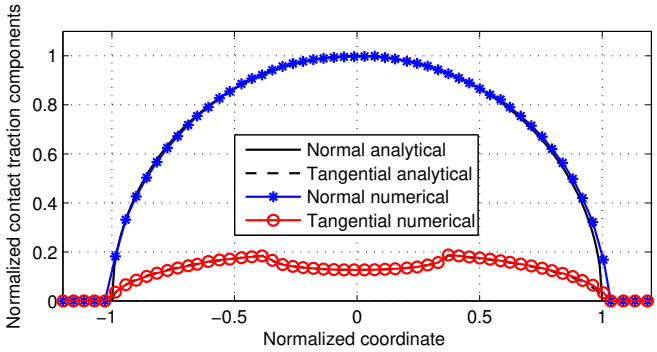

Figure 21. Analytical and numerical normalized contact traction components.

7.4. Sliding friction between deformable bodies

A half-cylindrical body is pressed onto an elastic slab and then moved in the tangential direction. The lower surface of the cylinder is treated as a slave. Neo-Hookean hyper-elastic material behaviour is assumed for both bodies, with material parameters $E = 1$ and $\nu = 0.3$ for the slab, and $E = 1000$ and $\nu = 0.3$ for the cylinder. The penalty parameters are $\epsilon_n = \epsilon_t = 100$ and the coefficient of friction is $\mu = 0.5$. The geometric model of the problem is illustrated in Fig. 22.

A uniform downward displacement U_y = -0.1 is applied to the upper face of the cylinder in 10 increments and then held constant while a horizontal displacement U_x = 2.0 is applied in 100 increments. Fig. 23 shows the contour plots for the stress field σ_{yy} in the deformed configuration for different load increments.

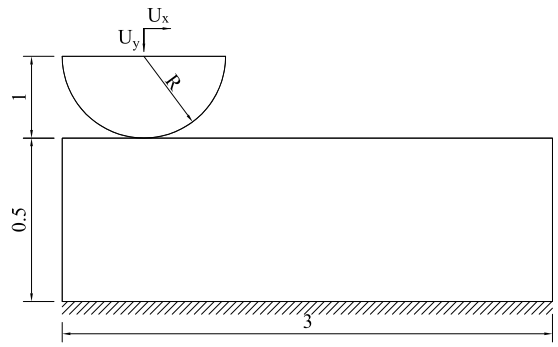

Figure 22. Geometrical configuration for sliding friction between deformable bodies.

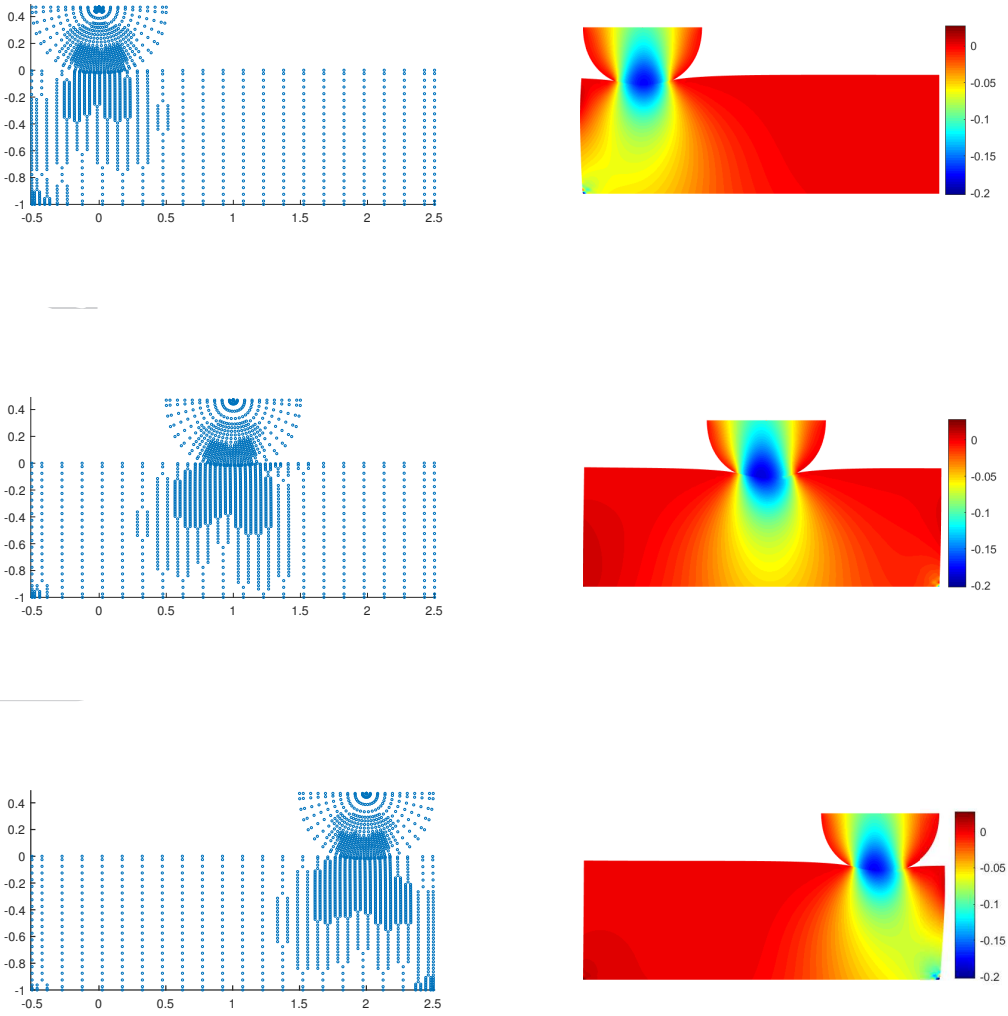

(a) (b)

Figure 23. (a) Adaptive mesh after 3 refinement steps and (b) the stress field contour plots for σ_{yy} at different time steps $t = 10, 50, 100$, respectively.

8. CONCLUSIONS

We have introduced an adaptivity in isogeometric meshfree collocation method for elasticity and friction contact problems. The present method was developed based upon a connection between the MLS-based meshfree shape functions and IGA basis functions to achieve the geometry exactness and the adaptive local refinement flexibility. Moreover, the resolution of the nonlinear contact governing equation is derived from a strong form to avoid the disadvantages of numerical integration. Numerical examples have shown that the present method has not only obtained stable and accurate results but has also been successfully implemented for the adaptive analysis. The convergence studies have also proven that the present method offers spatial convergence as high as that of the Galerkin finite element. Based on results obtained in this investigation, we have observed that:

- The present method has successfully demonstrated its advantages in the adaptive analysis. The gradient based error estimation strategy has also proved its robustness for the improvement of computational efficiency.
- The total number of unknowns in the present method equals those in the direct isogeometric collocation method, so the present method does not increase the computational cost significantly. The computational efficiency of adaptive refinement is higher than that of standard uniform refinement in terms of CPU time.
- The integrals were evaluated directly in the parametric space following the framework of IGA. Therefore, the implementation of the proposed method is simplified, and the computational effort is reduced.
- The comparison of the obtained results with an analytical solution for the Hertzian contact problem showed a good agreement and demonstrated the feasibility of the present method for treating the contact incompatible points. A high convergence rate was also achieved by the present method when compared with isogeometric collocations in uniform and non-uniform refinement.
- A large deformation and large sliding frictional ironing example has led to remarkably smooth global traction histories in both the normal and tangential directions.

ACKNOWLEDGMENTS

The authors acknowledge the financial support from the SMRT-NTU Smart Urban Rail Corporate Laboratory with funding support from the National Research Foundation, SMRT and Nanyang Technological University (Grant No. M4061892).

APPENDIX A: DERIVATIVES OF SHAPE FUNCTIONS

The first derivatives of shape function can be obtained from Eq. (19)

$$\begin{aligned}\phi_{i,\alpha}(\xi) =& \boldsymbol{p}^T\left(\xi_i^{[\cdot]}\right)\left[\boldsymbol{C}_{,\alpha}^{-1}(\xi)\,\boldsymbol{p}(\xi)\,\hat{W}\left(\xi-\xi_i^{[1]}\right)+\boldsymbol{C}^{-1}(\xi)\,\boldsymbol{p}_{,\alpha}(\xi)\,\hat{W}\left(\xi-\xi_i^{[1]}\right)\right.\\ &\left.+\,\boldsymbol{C}^{-1}(\xi)\,\boldsymbol{p}(\xi)\,\hat{W}_{,\alpha}\left(\xi-\xi_i^{[1]}\right)\right]\end{aligned}$$

The second derivatives of shape function are given

$$\begin{aligned}\phi_{i,\alpha\beta}(\xi) =& \boldsymbol{p}^T\left(\xi_i^{[\cdot]}\right)\Big[\boldsymbol{C}_{,\alpha\beta}^{-1}(\xi)\,\boldsymbol{p}(\xi)\,\hat{W}\left(\xi-\xi_i^{[1]}\right)+\boldsymbol{C}_{,\alpha}^{-1}(\xi)\,\boldsymbol{p}_{,\beta}(\xi)\,\hat{W}\left(\xi-\xi_i^{[1]}\right)\\ &+\boldsymbol{C}_{,\alpha}^{-1}(\xi)\,\boldsymbol{p}(\xi)\,\hat{W}_{,\beta}\left(\xi-\xi_i^{[1]}\right)+C_{,\beta}^{-1}(\xi)\,\boldsymbol{p}_{,\alpha}(\xi)\,\hat{W}\left(\xi-\xi_i^{[1]}\right)\\ &+\boldsymbol{C}^{-1}(\xi)\,\boldsymbol{p}_{,\alpha\beta}(\xi)\,\hat{W}\left(\xi-\xi_i^{[1]}\right)+\boldsymbol{C}^{-1}(\xi)\,\boldsymbol{p}_{,\alpha}(\xi)\,\hat{W}_{,\beta}\left(\xi-\xi_i^{[1]}\right)\\ &+\boldsymbol{C}_{,\beta}^{-1}(\xi)\,\boldsymbol{p}(\xi)\,\hat{W}_{,\alpha}\left(\xi-\xi_i^{[1]}\right)+\boldsymbol{C}^{-1}(\xi)\,\boldsymbol{p}_{,\beta}(\xi)\,\hat{W}_{,\alpha}\left(\xi-\xi_i^{[1]}\right)\\ &+\boldsymbol{C}^{-1}(\xi)\,\boldsymbol{p}(\xi)\,\hat{W}_{,\alpha\beta}\left(\xi-\xi_i^{[1]}\right)\Big]\end{aligned}$$

where $\boldsymbol{C}_{,\alpha}^{-1}=-\boldsymbol{C}^{-1}\boldsymbol{C}_{,\alpha}\boldsymbol{C}^{-1}$, and $\boldsymbol{C}_{,\alpha\beta}^{-1}=-\boldsymbol{C}^{-1}\left(\boldsymbol{C}_{,\alpha\beta}\boldsymbol{C}^{-1}+\boldsymbol{C}_{,\alpha}\boldsymbol{C}_{,\beta}^{-1}+\boldsymbol{C}_{,\beta}\boldsymbol{C}_{,\alpha}^{-1}\right)$.

APPENDIX B: LINEARIZATION OF THE CONTACT VARIABLES

The linearization of the normal gap is as follows ([45, 46, 36])

$$\Delta g_n=(\Delta\mathbf{x}^s-\Delta\bar{\mathbf{x}}^m)\cdot\mathbf{n}^m$$

The linearization of the contact traction from Eq. (42)

$$\Delta\mathbf{p}=-\Delta p_n\mathbf{n}^m-p_n\Delta\mathbf{n}^m+\Delta p_t^1\boldsymbol{\tau}_1^m+p_t^1\Delta\boldsymbol{\tau}_1^m$$

The variation of the normal $\Delta\mathbf{n}^m$ is given by

$$\Delta\mathbf{n}^m=-\left(\Delta\bar{\mathbf{x}}_{,\xi}^m\cdot\mathbf{n}^m+k_{11}^m\Delta\bar{\xi}^m\right)\boldsymbol{\tau}_1^{1m}=-\frac{1}{m_{11}}\left(\Delta\bar{\mathbf{x}}_{,\xi}^m\cdot\mathbf{n}^m+k_{11}^m\Delta\bar{\xi}^m\right)\boldsymbol{\tau}_1^m$$

in which

$$\Delta\bar{\xi}^m=\frac{1}{A_{11}^m}\left[(\Delta\mathbf{x}^s-\Delta\bar{\mathbf{x}}^m)\cdot\boldsymbol{\tau}_1^m+g_n\mathbf{n}^m\cdot\Delta\bar{\mathbf{x}}_{,\xi}^m\right]\tag{59}$$

$$A_{11}^m=m_{11}^m-g_nk_{11}^m$$

Substituting the expression of $\Delta\bar{\xi}^m$ into $\Delta\mathbf{n}^m$

$$\begin{aligned}\Delta\mathbf{n}^m&=-\left\{\tfrac{1}{m_{11}^m}\Delta\bar{\mathbf{x}}_{,\xi}^m\cdot\mathbf{n}^m+\tfrac{k_{11}^m}{A_{11}^m m_{11}^m}\left[(\Delta\mathbf{x}^s-\Delta\bar{\mathbf{x}}^m)\cdot\boldsymbol{\tau}_1^m+g_n\mathbf{n}^m\cdot\Delta\bar{\mathbf{x}}_{,\xi}^m\right]\right\}\boldsymbol{\tau}_1^m\\ &=-\left\{\tfrac{A_{11}^m+k_{11}^m g_n}{A_{11}^m m_{11}^m}\mathbf{n}^m\cdot\Delta\bar{\mathbf{x}}_{,\xi}^m+\tfrac{k_{11}^m}{A_{11}^m m_{11}^m}(\Delta\mathbf{x}^s-\Delta\bar{\mathbf{x}}^m)\cdot\boldsymbol{\tau}_1^m\right\}\boldsymbol{\tau}_1^m\\ &=-\left\{C_1\mathbf{n}^m\cdot\Delta\bar{\mathbf{x}}_{,\xi}^m+C_2(\Delta\mathbf{x}^s-\Delta\bar{\mathbf{x}}^m)\cdot\boldsymbol{\tau}_1^m\right\}\boldsymbol{\tau}_1^m\end{aligned}$$

where

$$C_1=\frac{A_{11}^m+k_{11}^m g_n}{A_{11}^m m_{11}^m}\;;\quad C_2=\frac{k_{11}^m}{A_{11}^m m_{11}^m}$$

Linearization of the traction in sticking from Eq. (45)

$$\Delta p_t^1=\Delta p_t^{1\text{trial}}=\varepsilon_t\Delta\bar{\xi}^m=\frac{\varepsilon_t}{A_{11}^m}\left[(\Delta\mathbf{x}^s-\Delta\bar{\mathbf{x}}^m)\cdot\boldsymbol{\tau}_1^m+g_n\mathbf{n}^m\cdot\Delta\bar{\mathbf{x}}_{,\xi}^m\right]$$

Linearization in case of sliding

$$\Delta p_t^1=-\mu\Delta p_n\frac{p_t^{1\text{trial}}}{\left\|\mathbf{p}_t^{\text{trial}}\right\|}-\mu p_n\frac{\Delta p_t^{1\text{trial}}}{\left\|\mathbf{p}_t^{\text{trial}}\right\|}+\mu p_n p_t^{1\text{trial}}\cdot\frac{\Delta\left\|\mathbf{p}_t^{\text{trial}}\right\|}{\left\|\mathbf{p}_t^{\text{trial}}\right\|^2}\tag{60}$$

where

$$\Delta \left\|\mathbf{p}_t^{\text{trial}}\right\| = \frac{\mathbf{p}_t^{\text{trial}} \cdot \Delta \mathbf{p}_t^{\text{trial}}}{\left\|\mathbf{p}_t^{\text{trial}}\right\|}$$

$$\Delta \mathbf{p}_t^{\text{trial}} = \Delta p_t^{1\text{trial}} \cdot \boldsymbol{\tau}_1^m + p_t^{1\text{trial}} \cdot \Delta \boldsymbol{\tau}_1^m$$

$$\Delta \boldsymbol{\tau}_1^m = \Delta \bar{\mathbf{x}}_{,\xi}^m + \mathbf{x}_{,\xi\xi}^m \Delta \bar{\xi}^m \tag{61}$$

Substituting Equation (59) into Equation (61), it follows

$$\Delta \boldsymbol{\tau}_1^m = \Delta \bar{\mathbf{x}}_{,\xi}^m + \frac{\mathbf{x}_{,\xi\xi}^m}{A_{11}^m} \left[(\Delta \mathbf{x}^s - \Delta \bar{\mathbf{x}}^m) \cdot \boldsymbol{\tau}^m + g_n \mathbf{n}^m \cdot \Delta \bar{\mathbf{x}}_{,\xi}^m \right]$$

Equation Equation (60) can be rewritten as

$$\Delta p_t^1 = -\frac{\mu}{\left\|\mathbf{p}_t^{\text{trial}}\right\|} \left(p_t^{1\text{trial}} \cdot \Delta p_n + p_n \cdot \Delta p_t^{1\text{trial}} - \frac{p_n p_t^{1\text{trial}} \cdot \Delta \left\|\mathbf{p}_t^{\text{trial}}\right\|}{\left\|\mathbf{p}_t^{\text{trial}}\right\|} \right)$$

with

$$\Delta \left\|\mathbf{p}_t^{\text{trial}}\right\| = \frac{\mathbf{p}_t^{\text{trial}}}{\left\|\mathbf{p}_t^{\text{trial}}\right\|} \cdot \left(\Delta p_t^{1\text{trial}} \cdot \boldsymbol{\tau}_1^m + p_t^{1\text{trial}} \cdot \Delta \boldsymbol{\tau}_1^m \right)$$

REFERENCES

1. T. Belytschko, Y.Krongauz, D.Organ, M.Fleming, and P.Krysl. Meshless methods: An overview and recent developments. *CMAME*, 39:3–47, 1996.
2. S. Li, W. Hao, and W.K. Liu. Numerical simulations of large deformation of thin shell structures using meshfree methods. *Computational Mechanics*, 25:102–116, 2000.
3. S. Li, D. Qian, W.K. Liu, and T. Belytschko. A meshfree contact-detection algorithm. *CMAME*, 190:3271–3292, 2001.
4. T. Belytschko, Y.Y.Lu, and L.Gu. Element-free Galerkin methods. *IJNME*, 37(2):229–256, 1994.
5. T. Rabczuk, S.P. Xiao, and M. Sauer. Coupling of meshfree methods with finite elements: Basic concepts and test results. *CNME*, 22:1031–1065, 2006.
6. T. Rabczuk and G. Zi. A meshfree method based on the local partition of unity for cohesive cracks. *Computational Mechanics*, 39:743–760, 2007.
7. T.J.R. Hughes, J.A. Cottrell, and Y. Bazilevs. Isogeometric analysis: CAD, finite elements, NURBS, exact geometry and mesh refinement. *CMAME*, 194:4135–4195, 2005.
8. L. De Lorenzis, I. Temizer, P. Wriggers, and G. Zavarise. A large deformation frictional contact formulation using nurbs-based isogeometric analysis. *IJNME*, 87:1278–1300, 2011.
9. L. De Lorenzis, P. Wriggers, and G. Zavarise. A mortar formulation for 3d large deformation contact using NURBS-based isogeometric analysis and the augmented Lagrangian method. *CM*, 49:1–20, 2012.
10. L. De Lorenzis, P. Wriggers, and TJR Hughes. Isogeometric contact: a review. *GAMM-Mitteilungen*, 37:85–123, 2014.
11. R. Dimitri, L. De Lorenzis, M.A. Scott, P. Wriggers, R.L. Taylor, and G. Zavarise. Isogeometric large deformation frictionless contact using T-splines. *CMAME*, 269:394–414, 2014.
12. R. Dimitri, L. De Lorenzis, P. Wriggers, and G. Zavarise. NURBS and T-spline-based isogeometric cohesive zone modeling of interface debonding. *CM*, 54:369–388, 2014.
13. I. Temizer, P. Wriggers, and T.J.R. Hughes. Contact treatment in isogeometric analysis with NURBS. *CMAME*, 200:1100–1112, 2011.
14. S. Lipton, J.A Evans, Y. Bazilevs, T. Elguedj, and T.J.R. Hughes. Robustness of isogeometric structural discretizations und severe mesh distortion. *Computer Methods in Applied Mechanics and Engineering*, 199:357–373, 2010.
15. Y. Bazilevs, V.M. Calo, J.A. Cottrell, J.A. Evans T.J.R Hughes, S. Lipton, and M.A. Scottand T.W. Sederberg. Isogeometric analysis using T-splines. *Computer Methods in Applied Mechanics and Engineering*, 199:229–263, 2010.
16. M. Dörfel, B. Juttler, and B. Simeon. Adaptive isogeometric analysis by local h-refinement with T-splines. *CMAME*, 199:264–275, 2010.
17. N. Nguyen-Thanh, H. Nguyen-Xuan, S. Bordas, and T. Rabczuk. Isogeometric analysis using polynomial splines over hierarchical T-meshes for two-dimensional elastic solids. *CMAME*, 200(21-22):1892–1908, 2011.
18. N. Nguyen?Thanh and K. Zhou. Extended isogeometric analysis based on PHT-splines for crack propagation near inclusions. *IJNME*, 112:1777–1800, 2017.

19. N. Nguyen-Thanh, K.Zhou, X.Zhuang, P.Areias, H.Nguyen-Xuan, Y.Bazilevs, and T.Rabczuk. Isogeometric analysis of large-deformation thin shells using RHT-splines for multiple-patch coupling. *Computer Methods in Applied Mechanics and Engineering*, 316:1157–1178, 2017.
20. D. Schillinger, L. Dede, M.A. Scott, J.A. Evans, M.J. Borden, E. Rank, and T.J.R. Hughes. An isogeometric design-through-analysis methodology based on adaptive hierarchical refinement of NURBS, immersed boundary methods, and T-spline CAD surfaces. *CMAME*, 249-252:116–150, 2012.
21. A.-V. Vuong, C. Giannelli, B. Jüttler, and B. Simeon. A hierarchical approach to adaptive local refinement in isogeometric analysis. *CMAME*, 200:3554–3567, 2012.
22. K.A. Johannessen, T. Kvamsdal, and T. Dokken. Isogeometric analysis using LR B-splines. *CMAME*, 269:471–514, 2014.
23. R. de Borst and L. Chen. The role of Bezier extraction in adaptive isogeometric analysis: Local refinement and hierarchical refinement. *IJNME*, 113:999–1019, 2018.
24. L. Chen and R. de Borst. Adaptive refinement of hierarchical t-splines. *CMAME*, 337:220–245, 2018.
25. F. Auricchio, L. Beirao da Veiga, T.J.R. Hughes, A. Reali, and G.Sangalli. Isogeometric collocation for elastostatics and explicit dynamics. *CMAME*, 14(2):249–252, 2014.
26. A. Reali and H. Gomez. An isogeometric collocation approach for Bernoulli-Euler beams and Kirchhoff plates. *CMAME*, 284:623–636, 2015.
27. J. Kiendl, F.Auricchio, L.Beirao da Veiga, C.Lovadina, and A.Reali. Isogeometric collocation methods for the reissner-mindlin plate problem. *CMAME*, 284:489–507, 2015.
28. C. Anitescu, Y. Jia, Y.J. Zhang, and T. Rabczuk. An isogeometric collocation method using superconvergent points. *CMAME*, 284:1073–1097, 2015.
29. D. Schillinger, S.J. Hossain, and T.J.R. Hughes. Reduced bezier element quadrature rules for quadratic and cubic splines in isogeometric analysis. *CMAME*, 277:1–45, 2014.
30. D. Schillinger, J.A. Evans, A. Reali, M.A. Scott, and T.J.R. Hughes. Isogeometric collocation: Cost comparison with galerkin methods and extension to adaptive hierarchical nurbs discretizations. *CMAME*, 267:170–232, 2013.
31. J.S. Chen and H.P. Wang. New boundary condition treatments in meshfree computation of contact problems. *CMAME*, 187:441–468, 2000.
32. R.A. Sauer and S. Li. A contact mechanics model for quasi?continua. *IJNME*, 71:931–962, 2007.
33. R.A. Sauer and S. Li. An atomistically enriched continuum model for nanoscale contact mechanics and its application to contact scaling. *Journal of nanoscience and nanotechnology*, 8:3757–3773, 2008.
34. S. Li, Q.Yao, Q.Li, X.Q.Feng, and H.Gao. Contact stiffness of regularly patterned multi-asperity interfaces. *Journal of the Mechanics and Physics of Solids*, 111:277–289, 2018.
35. L. De Lorenzis, J.A. Evans, T.J.R. Hughes, and A. Reali. Isogeometric collocation: Neumann boundary conditions and contact. *CMAME*, 284:21–54, 2015.
36. R.Kruse, N.Nguyen-Thanh, L.De Lorenzis, and T.J.R.Hughes. Isogeometric collocation for large deformation elasticity and frictional contact problems. *CMAME*, 296:73–112, 2015.
37. R.A. Sauer and L. De Lorenzis. A computational contact formulation based on surface potentials. *CMAME*, 253:369–395, 2013.
38. R.A. Sauer and L. De Lorenzis. An unbiased computational contact formulation for 3d friction. *IJNME*, 2014.
39. D. Levin. The approximation power of moving least-squares. *Mathematics of Computation of the American Mathematical Society*, 67(224):1517–1531, 1998.
40. S. Li and W.K. Liu. Moving least-square reproducing kernel method Part II: Fourier analysis. *CMAME*, 139:159–193, 1996.
41. Y. Luo and U. Haussler-Combe. An adaptivity procedure based on the gradient of strain energy density and its application in meshless methods. *Meshfree Methods for Partial Differential Equations*, 26:267–279, 2003.
42. S.P. Timoshenko and J.N. Goodier. *Theory of Elasticity (3rd edn)*. McGraw, New York, 1970.
43. D. Nowell, D.A. Hills, and A. Sackfield. Contact of dissimilar elastic cylinders under normal and tangential loading. *Journal of the Mechanics and Physics of Solids*, 36:59–75, 1988.
44. D.A. Hills and D. Nowell. *Mechanics of Fretting Fatigue*. Kluwer Academic Publishers, Dordrecht, 1994.
45. T.A. Laursen. *Computational Contact and Impact Mechanics*. Springer, Berlin, 2002.
46. P. Wriggers. *Computational Contact Mechanics (2nd edn)*. Springer, Berlin, 2006.